Near-Zero Drift and High Electromechanical Coupling Acoustic Resonators at >3.5 GHz

Ahmed E. Hassanien, *Student Member, IEEE*, Ruochen Lu, *Member, IEEE*, and Songbin Gong, *Senior Member, IEEE*

***Abstract*— In this article, near-zero drift and high electromechanical coupling acoustic resonators have been designed and demonstrated. The acoustic resonator is based on Lamb acoustic waves in a bimorph composed of lithium niobate on silicon dioxide. Our approach breaks through a performance boundary in conventional Lamb-wave resonators by introducing the bimorph while operating at higher order resonant modes. This enables the resonator to achieve frequency scalability, a low-temperature coefficient of frequency, and high electromechanical coupling altogether. The electromechanical coupling and temperature coefficient of the resonator were analytically optimized for the A_3 mode through adjusting the thicknesses of different materials in the bimorph. Resonators with different dimensions and stack thickness were fabricated and measured, resulting in a temperature coefficient of frequency ranging from −17.6 to −1.1 ppm/°C, high electromechanical coupling ranging from 13.4% to 18%, and quality factors up to 800 at 3.5 GHz. The achieved specifications are adequate for fifth-generation (5G) sub-6-GHz frequency bands n77 and n78.**

***Index Terms*— Acoustic resonators, fifth generation (5G), lithium niobate on insulator (LNOI), low-temperature coefficient of frequency (TCF), microelectromechanical systems (MEMS), new radio (NR), piezoelectricity.**

I. Introduction

THE fifth-generation mobile network (5G) is a global wireless standard advancing the prevalent connectivity between people, machines, and devices [1], [2]. The third-generation partnership project (3GPP), a collective project partnership of mobile system manufacturers, has played a critical role in the development and deployment of the 5G standard [1]. Specifically, 5G new radio (NR) uses modulation schemes, waveforms, and access technologies, enabling increased data rates, coverage, reliability, capacity, and low latency [2]. 5G is driven by consumers and industrial trends, such as enhanced mobile broadband (eMBB), Internet of Things (IoT), smart vehicles, and healthcare/critical services [3], [4]. eMBB, which is the main focus of the 5G NR, imposes a constant demand for higher data rates in an increasingly crowded spectrum [3], [5], [6]. Radio frequency (RF) front ends are now required to coexist with tighter spectral spacing while operating at higher frequencies and over larger bandwidths. Unsurprisingly, these place progressively stringent conditions on the mobile front-end filters for maintaining temperature stability, frequency scalability, and wideband compatibility. It is undoubtedly a high order as achieving all three requires overcoming the unforgiving design trades that filter designers face every day using incumbent resonator technologies.

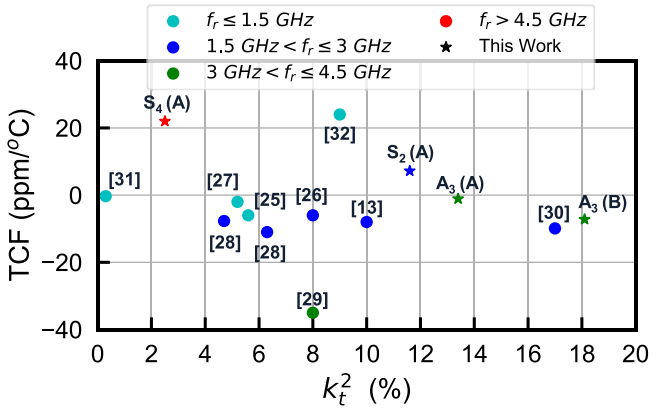

Fig. 1. Resonators performance comparison including the work presented in this article. All modes of device A are shown and A_3 mode only for device B. Reference numbers are between brackets and device names are between parentheses.

The incumbent mobile filters are based on either surface acoustic waves (SAWs) [7], [8] or bulk acoustic waves (BAWs) [9], [10]. SAW resonators have electromechanical coupling k_t^2 < 10%, temperature coefficient of frequency (TCF) of ±44 ppm/°C, and diminishing performance beyond 2.7 GHz [11]. On the other hand, conventional BAW resonators on aluminum nitride (AlN) can be scaled to higher frequencies (>5 GHz) with TCF ∼ −30 ppm/°C and k_t^2 around 6% [12]. Despite their different technical strengths, improving any of the three specifications for either SAW or BAW often means compromising the other two. For instance, temperature-compensated SAW (TCSAW) uses SiO_2 to reduce TCF at the expense of lowering k_t^2 and attainable bandwidth [12], [13]. BAW adopts doped AlN [14] to raise k_t^2 but unfortunately reduces phase velocity (hence frequency scalability) and increases TCF in the process.

Manuscript received February 1, 2021; revised March 10, 2021 and April 19, 2021; accepted April 25, 2021. Date of publication May 26, 2021; date of current version August 5, 2021. This work was supported by the NASA Early Career Faculty (ECF) Program. *(Corresponding author: Ahmed E. Hassanien.)*

Ahmed E. Hassanien and Songbin Gong are with the Department of Electrical and Computer Engineering, University of Illinois at Urbana–Champaign, Urbana, IL 61801 USA (e-mail: ahmedeh2@illinois.edu).

Ruochen Lu was with the Department of Electrical and Computer Engineering, University of Illinois at Urbana–Champaign, Urbana, IL 61801 USA. He is now with the Department of Electrical and Computer Engineering, University of Texas at Austin, Austin, TX 78712 USA.

Color versions of one or more figures in this article are available at https://doi.org/10.1109/TMTT.2021.3079497.

Digital Object Identifier 10.1109/TMTT.2021.3079497

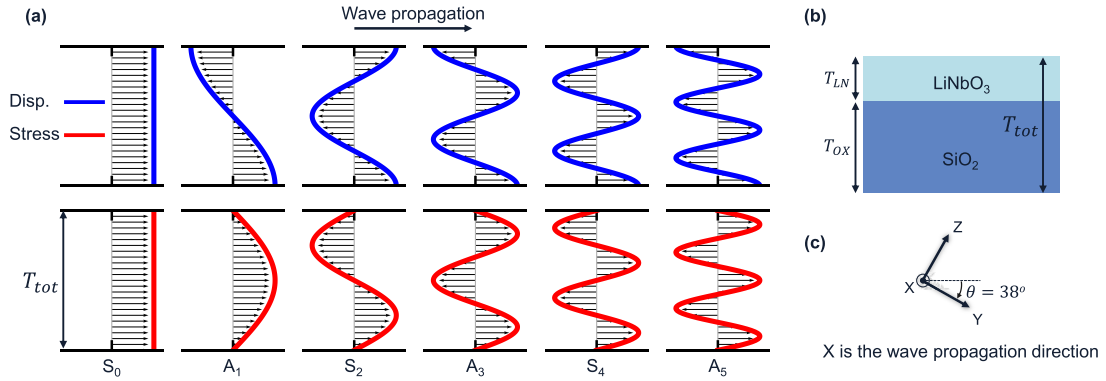

Fig. 2. (a) Displacement following arrows direction (top) and stress (bottom) distribution in thickness direction for the first three even-order symmetric modes (S_n) and odd-order antisymmetric modes (A_m) that can be excited using lateral electric fields with top-only electrodes. (b) Proposed bimorph made of $LiNbO_3$ and SiO_2 where the thickness of different materials can be optimized based on the targeted resonant mode. (c) Lithium niobate orientation (128° Y-cut) resulting in maximum electromechanical coupling to shear waves using lateral electric fields excitation.

Recent research on Lamb-wave devices based on lithium niobate ($LiNbO_3$) promises an alternative to SAW and BAW [15]–[21], particularly for wideband applications at high center frequencies. These approaches leverage the large k_t^2 in $LiNbO_3$ and overmoding to beyond 3 GHz with excellent performance. Nonetheless, further attempts to improve their high TCF (−70 ppm/°C) and loss of k_t^2 from overmoding led so far to a frustrating zero-sum game [20], [22]–[24], similarly seen in SAW and BAW [13], [25]. The outcome of these attempts is shown in Fig. 1, showing the performance boundaries of the best TCSAW [13], [26], [27], TCBAW [25], [28], and Lamb-waves devices [29]–[32] compared to our work (devices A and B) in this article. Note that in Fig. 1, many devices with low electromechanical coupling were designed to achieve specific bandwidth requirements. Some of them can achieve higher electromechanical coupling. For full performance comparison, other metrics, such as quality factor or impedance ratio, should be included.

Compared to the IHP SAW [13], our proposed resonator utilizes the same functional layer made of SiO_2 for temperature compensation, as shown in Fig. 1. Unlike IHP, Lamb waves allow for a much faster phase velocity and hence operation at higher frequencies that exceed IHP demonstrations (currently around 2.7 GHz using i-line lithography). Moreover, Lamb-wave modes show higher electromechanical coupling than IHP, promising wider bandwidth and potentially higher figure of merit. On the other hand, IHP SAW technology is a solidly mounted structure allowing for a thermal path to the substrate, consequently, better power handling capability, in addition to the higher quality factor.

In order to transcend the unfavorable tradeoff between k_t^2 and TCF, we utilize a bimorph instead of a single material in conventional Lamb-wave resonators [20], [22]–[24]. The stack is made of $LiNbO_3$ on top of SiO_2 [33]. $LiNbO_3$ has a negative temperature coefficient of elastic and piezoelectric constants, while SiO_2 has the opposite [34]. Selecting the right thicknesses for different materials in the bimorph could result in a zero TCF resonator. Although this is not news in resonator design, the designed bimorph herein unconventionally improves TCF while not giving up k_t^2. To do so, we adopt a higher order mode (A_3) so that the overlap between the stress and the applied electric fields across the bimorph increases (resulting in larger k_t^2), while temperature compensation is induced by the SiO_2 layer in the bimorph. In essence, such a design produces a trio of benefits, namely improving TCF and k_t^2 and increasing center frequency all at once.

This article is an extension of [35], which reports only the measurement of one of the resonators reported in this article (device A). This article has included a detailed theoretical approach for designing the multilayer resonator, selecting the piezoelectric substrate orientation, and understanding key design parameters. Additional results on fabricated and measured devices with higher k_t^2 are included, leading to a further discussion on improving the performance of the proposed resonator. This work's most representative device shows an ultralow TCF of −1.1 ppm/°C, a high electromechanical coupling of 13.5%, and a 500-quality factor at 3.5 GHz. By comparing this result with others in Fig. 1, we see that our approach breaks through a performance boundary that previously held back others.

The rest of this article is organized as follows. Section II explores the design methodology, focusing on the theoretical approach, finite-element analysis (FEA) optimization, and simulation results. Section III shows the steps to validate the investigated concepts, including the fabrication process and measurement results. Further enhancements are discussed in Section IV followed by the conclusion in Section V.

II. Design Methodology

A. Theory

To help explain the theoretical approach, we assume a suspended thin-film substrate with a total thickness T_{tot} made of an arbitrary number of materials with similar mechanical properties and wave velocities, allowing Lamb waves to propagate with minimal distortion. Fig. 2(a) shows the displacement and stress distributions in the suspended film thickness direction for the first three even-order symmetric (S) and odd-order antisymmetric (A) Lamb-wave resonant modes [36], [37]. The plotted resonant modes are the modes that can be efficiently excited by interdigital electrodes (IDTs) only on the top surface, which highly simplifies the fabrication

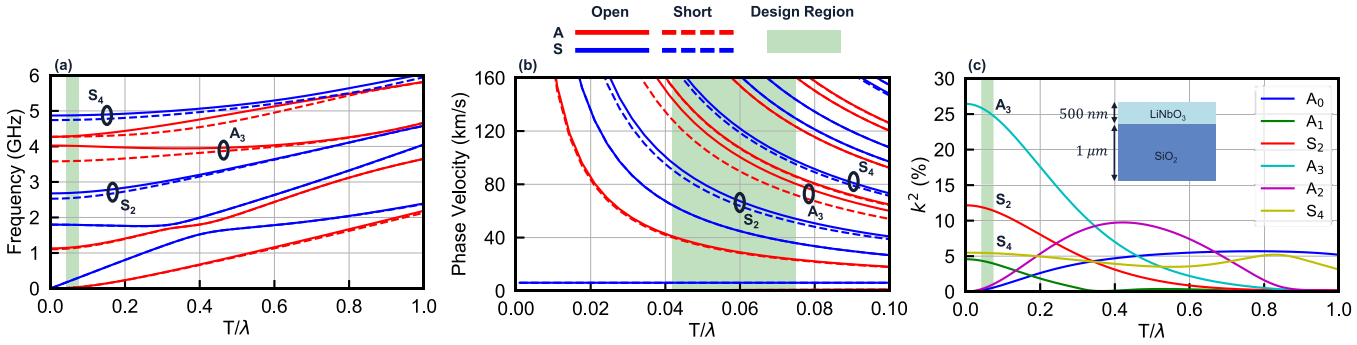

Fig. 3. Dispersion curves for a bimorph made of 500-nm $LiNbO_3$ on top of 1-μm SiO_2 resulting in $T = 1.5$ μm (a) versus frequency and (b) versus phase velocity. (c) Electromechanical coupling calculated knowing the phase velocity with electrical open and short boundary conditions on the top surface. A: asymmetric modes. S: symmetric modes.

process [23]. The number of displacement nodes within the film equals the mode order, whereas the number of stress nodes equals the mode order minus one (ignoring the two nodes at the edges). For fabrication simplicity, we optimize our resonator for the bimorph case. As shown in Fig. 2(b), the bimorph is made of $LiNbO_3$ and SiO_2. $LiNbO_3$ is a highly piezoelectric material with large electromechanical coupling for exciting the acoustic waves [38]. It has negative temperature coefficients of elastic and piezoelectric constants [34]. SiO_2 is an intermediate passive layer used in the lithium-niobate-on-insulator (LNOI) technology [39]. SiO_2 is usually used for temperature compensation as it has positive temperature coefficients of elastic constants [34].

To maximize k_t^2, we adopt Berlincourt's formulation for electromechanical coupling calculation. For maximum coupling, the mutual energy U_m needs to be maximized, which can be formulated as [40], [41]

$$U_m \propto \int (E.d.T)dV \tag{1}$$

where E, d, T, and V are the electric fields, the piezoelectric coefficient, stress, and volume of the piezoelectric material, respectively. Equation (1) signifies the importance of the overlap between the applied lateral electric fields and the stress distribution of the resonant mode inside the piezoelectric material in the thickness direction. For example, Fig. 2(a) shows that the stress distribution of the A_3 mode has two nodal points in the thickness direction. By choosing the thickness of $LiNbO_3$ to be half of SiO_2 thickness, the upper nodal point can be located at the interface between the two materials leaving half a sinusoid in $LiNbO_3$. This results in the maximum overlap between E and T. The piezoelectric constant d relevant to our device operation (the strain charge form of the piezoelectric constitutive equations) can also be maximized by selecting the appropriate device orientation in an optimal $LiNbO_3$ cut. In the case of A-modes, the optimal orientation is in the X-direction in 128° Y-cut, as shown in Fig. 2(c). In this orientation, maximum electromechanical coupling to shear waves, around 2 (in-plane axis) of Fig. 4(b), can be acquired as it features a high piezoelectric constant e_{15} of 4.47 C/m^2. e_{15} is the piezoelectric coefficient in the stress-charge form mapping the applied electric field in 1 to acoustic waves in 5 (shear around 2). Note that an asymmetric Lamb wave is composed of a longitudinal and transverse vertical waves coupled together to form a sagittally polarized wave. The direction of propagation is parallel to X or 1. For the A_3 mode, the resulting strain for the 2-D cavity resonator is predominately shear around 2 (strain component with index 5) where the 2-D cavity is defined by the metallic IDTs. Moreover, other piezoelectric constants, such as e_{11} and e_{16}, are almost zero resulting in minimal electromechanical coupling to longitudinal and shear horizontal waves and, therefore, spurious modes mitigation [24], [42]. Euler angles following the ZXZ convention in COMSOL are $\alpha = 0$, $\beta = -38$, and $\gamma = 0$ for 128° Y-cut [43] (0, 38, and 0 according to [44]).

While the film thicknesses can be optimized for maximum electromechanical coupling exclusively, they can also be tailored to minimize the TCF while maintaining high electromechanical coupling. Temperature coefficients for different materials constants used in this article can be found in [34]. The third-order antisymmetric mode A_3 has the best tradeoff between k_t^2 and TCF. It potentially has a zero TCF added to maximum overlap between the applied electric field and stress and, therefore, maximum coupling.

Dispersion curves can be generated using FEA eigenmode simulations as setup in [24] and [45]. Fig. 3(a) and (b) shows the dispersion curves of a bimorph made of 500-nm $LiNbO_3$ on top of 1-μm SiO_2 corresponding to a total thickness of 1.5 μm. The design region with T/λ ranging from 0.042 to 0.075 was selected, resulting in a large wavelength (λ) ranging from 20 up to 36 μm. This allows us to use standard optical lithography with large dimensions >2 μm. Although the dimensions are large, the resulting frequency of operation is still high ~3.5 GHz as the phase velocities are approximately 75, 112, and 136 km/s for S_2, A_3, and S_4 resonant modes, respectively. The expected electromechanical coupling is plotted in Fig. 3(c), which can be calculated as follows [46], [47]:

$$k^2 = \frac{v_o^2 - v_s^2}{v_s^2} \tag{2}$$

where v_o and v_s are the phase velocities calculated with eigenmode simulations of the bilayer stack with open and short electrical boundary conditions, respectively, on the top surface, without any mass loading from the electrodes.

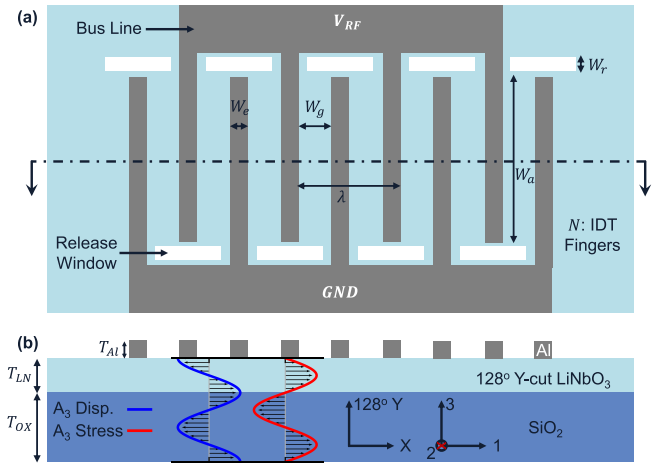

Fig. 4. Mock-up of the acoustic resonator. (a) Top view. (b) Cross-sectional view with displacement and stress distribution in the thickness direction of the A_3 mode.

TABLE I
SIMULATED DEVICE DIMENSIONS

Parameter	Value	Parameter	Value
N	9	W_e	3 μm
T_{LN}	0.5 μm	W_g	11 μm
T_{Ox}	1 μm	λ	28 μm
T_{Al}	0.25 μm	W_a	46 μm
W_r	5 μm		

B. A_3 Mode Acoustic Resonator Structure

Fig. 4 shows the basic structure of the A_3 bimorph resonator. The resonator body is composed of $LiNbO_3$ on top of SiO_2 with top Al interdigitated electrodes. For simplicity, the resonator can be modeled as a 2-D cavity where the energy is trapped between the thick electrodes. The center frequency can be determined from the thickness of the thin film and the lateral dimensions of the 2-D cavity [23]. The detailed analysis of Lamb modes in thin films is available in the literature [48], but because of its complex properties, numerical simulations are required for accurate frequency estimation. Film thicknesses in the bimorph are engineered to maximize electromechanical coupling, while the lateral dimensions are optimized for minimum possible spurious modes [23].

In order to verify the discussed theory, the proposed structure is simulated using FEA with the dimensions given in Table I. Fig. 5(a) shows the wideband simulated admittance of the Lamb-wave resonator along with different mode shapes for S_2, A_3, and S_4 in Fig. 5(b). Since the structure is optimized for A_3 mode, it results in a maximum k_t^2 of 21% and lower k_t^2 for other modes. k_t^2 used in this article is defined as $(\pi^2/8)((f_p^2/f_r^2) - 1)$, where f_r is the resonance frequency and f_p is the antiresonance frequency [49]. The A_3 mode has a resonant frequency around 3.6 GHz, which is applicable to 5G at the sub-6-GHz frequency bands.

Fig. 6 shows the simulated k_t^2 and TCF versus $LiNbO_3$ thickness for the A_3 mode. All TCF values throughout this article refer to the series resonance frequency shift and can be calculated using (6). The figure reveals the tradeoff

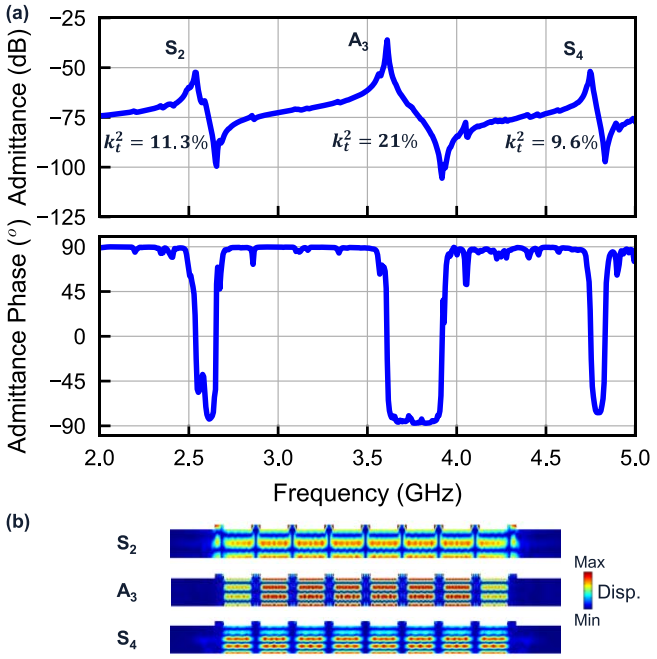

Fig. 5. FEA simulation of the proposed Lamb-wave resonator. (a) Admittance in magnitude (top) and phase (bottom). (b) Displacement (in 1 or X-direction) mode shapes of different resonant modes at the resonance frequency.

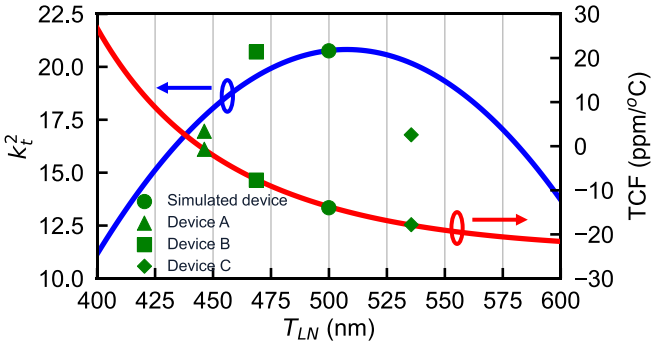

Fig. 6. Simulated k_t^2 and TCF of the proposed resonator versus $LiNbO_3$ thickness for the A_3 mode. Only $LiNbO_3$ thickness varies, while all other dimensions can be found in Table I. For every device, the bottom green marker presents TCF and the top green marker presents k_t^2.

between k_t^2 and TCF and suggests that k_t^2 more than 12% and TCF $< \pm 20$ ppm/°C can be attained simultaneously. Variations across the wafer are expected due to slight thickness variations of $LiNbO_3$, SiO_2, and Al. The tradeoff is mode-dependent, and similar figures can be generated for other modes.

Compared with conventional Lamb-waves resonators where higher order modes have low k_t^2 and high TCF, the proposed bimorph-based resonator allows for frequency scaling at much higher k_t^2 while improving TCF simultaneously. The gained enhancement is added to the ease of fabrication without any special processing techniques.

III. EXPERIMENTAL VALIDATION

To experimentally validate the proposed concepts in this article, a set of devices was fabricated using standard optical photolithography and then measured using a vector network analyzer (VNA). The wafer used in the fabrication has $LiNbO_3$, SiO_2, and Al thicknesses ranging from 480 to 545 nm, 0.94 to 1.06 μm, and 245 to 260 nm, respectively.

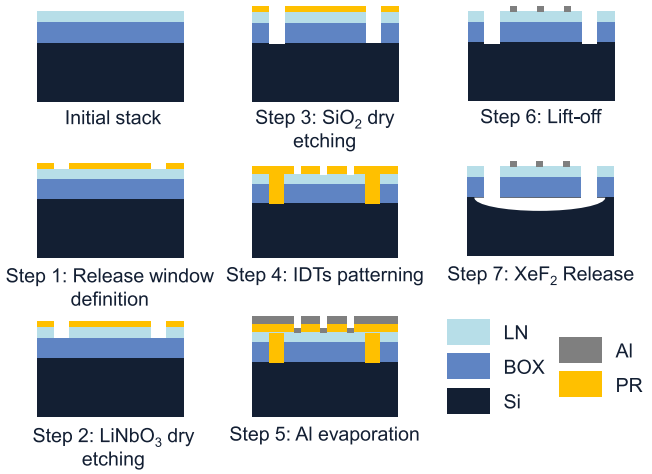

Fig. 7. Fabrication process.

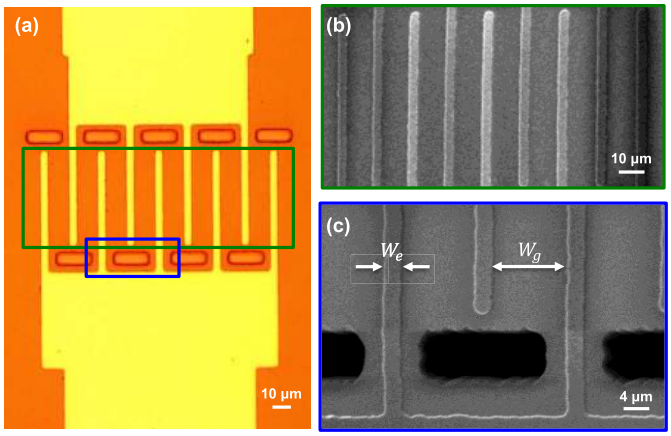

Fig. 8. (a) Microscope image of the fabricated device A. (b) Zoomed-in view SEM image of the IDTs. (c) Zoomed-in view SEM of the etched release windows.

A. Fabrication Process

The fabrication process steps are shown in Fig. 7. The fabrication process starts with transfer bonding a 128° Y-cut single-crystal $LiNbO_3$ thin film (0.5 μm) to a silicon carrier (500 μm) with an intermediate layer of SiO_2 (1 μm) using the ion-slicing technique [50]. Next, a photoresist layer is spun and patterned using optical lithography as the soft mask for defining the release windows. Inductively coupled plasma with Ar-based reactive ion etching is then used to etch through $LiNbO_3$ and SiO_2. After that, the IDTs are defined by lifting-off 250-nm evaporated Al. Finally, the resonator is released by using XeF_2 isotropic etching to remove the silicon underneath the bimorph. Fig. 8 shows a microscope image and scanning electron microscope (SEM) images of device A.

B. Measurements

Three resonators with different lateral dimensions were measured using VNA first at room temperature and then at various elevated temperatures up to 75 °C. The measured devices were chosen randomly from the fabricated wafer to reflect thickness variation effects. Resonators' lateral dimensions are detailed in Table II.

TABLE II
DESIGN PARAMETERS OF MEASURED DEVICES

Device	N	W_e	W_g	λ	W_a
A	9	3 μm	11 μm	28 μm	46 μm
B	15	3 μm	7 μm	20 μm	46 μm
C	5	3 μm	8 μm	22 μm	76 μm

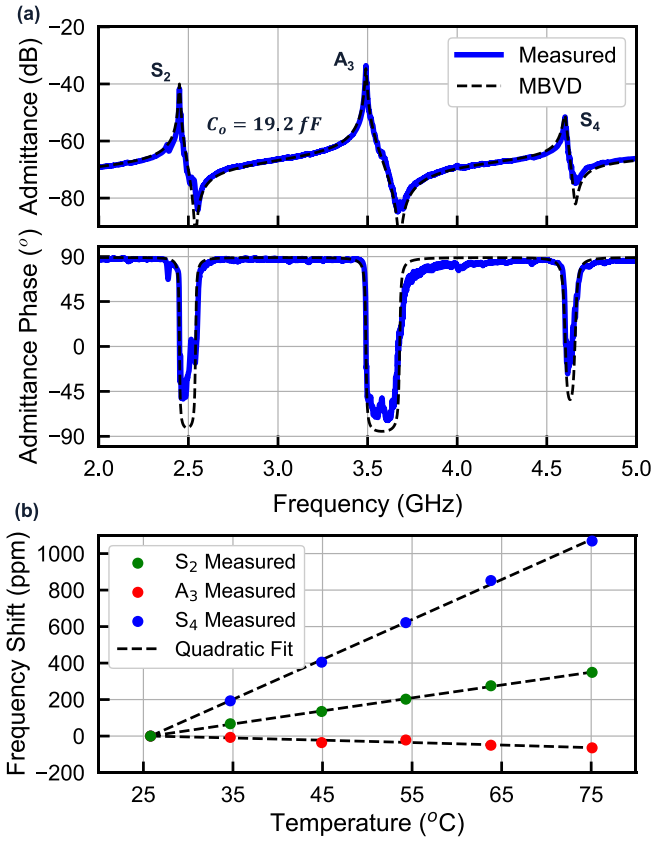

Fig. 9. Measurements of device A. (a) Admittance in magnitude (top) and phase (bottom) along with their MBVD fit. (b) Frequency shift of the acoustic resonator versus temperature for different modes with their quadratic fit used to calculate TCF.

Fig. 9(a) shows the measured admittance of device A at room temperature along with the modified Butterworth–Van Dyke (MBVD) model result [49]. The MBVD fit is used to extract different resonator parameters and its multiresonance equivalent circuit can be found in Fig. 10. For each resonant mode, a series resonance branch composed of a motional resistance (R_m), inductance (L_m), and capacitance (C_m) can be calculated as follows:

$$R_m = \frac{\pi^2}{8} \cdot \frac{1}{\omega_r C_0} \cdot \frac{1}{k_t^2 Q} \tag{3}$$

$$L_m = \frac{\pi^2}{8} \cdot \frac{1}{\omega_r^2 C_0} \cdot \frac{1}{k_t^2} \tag{4}$$

$$C_m = \frac{8}{\pi^2} \cdot C_0 k_t^2 \tag{5}$$

where C_o represents the static capacitance between the input terminals comprising the IDTs and the feedthrough capacitances, Q is the mode quality factor, and ω_r is the angular resonant frequency.

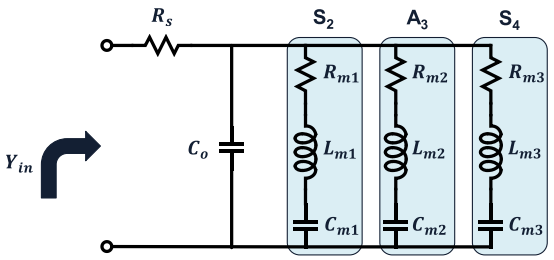

Fig. 10. Equivalent MBVD model including a series parasitic resistance R_s, a static capacitance C_o, and a series resonant (RLC) branch representing each resonant mode. Y_{in} is the total input admittance.

TABLE III
EXTRACTED PARAMETERS OF DEVICE A

Mode	f_r (GHz)	Q	k_t^2 (%)	TCF (ppm/°C)	TCF_2 (ppm/°C^2)
S_2	2.45	400	11.6	7.2	0.0
A_3	**3.49**	**500**	**13.5**	**-1.1**	**0.0**
S_4	4.6	250	2.5	22	0.0

The measured A_3 mode for device A shows resonance at 3.5 GHz and $k_t^2 = 13.5\%$. The measured k_t^2 value deviates from the simulation for two reasons: 1) thickness variations and 2) the feedthrough capacitance. The device is expected to have $k_t^2 \sim 16.5\%$ after deembedding a capacitance of 4 fF representing the feedthrough effect verifying the simulations in Fig. 6. The feedthrough capacitance was measured using identical deembedding structures to the resonator without the IDTs to measure the capacitance through the substrate.

Fig. 9(b) shows the measured resonant frequency deviation for device A in ppm with respect to its value at room temperature (25 °C). Measured values are then quadratically fit to extract the first- and second-order TCFs using the following equation:

$$\Delta f/f = \text{TCF} \times \Delta T + \text{TCF}_2 \times \Delta T^2 \tag{6}$$

where $\Delta f/f$ is the frequency shift in ppm, TCF is the linear TCF in ppm/°C, TCF_2 is the second-order TCF in ppm/°C^2, and $\Delta T = T - T_o$ is the temperature shift from a reference temperature value T_o (room temperature). Table III summarizes the extracted parameters for device A.

Fig. 11(a) shows the measured admittance of device B at room temperature along with the MBVD model fit. The measured A_3 mode shows a resonance at 3.5 GHz and high $k_t^2 = 18.1\%$. The measured k_t^2 value is expected to be even higher $\sim 20.5\%$ after deembedding a capacitance of 4 fF. Fig. 11(b) shows the measured resonant frequency deviation for device B in ppm with respect to its value at room temperature. Table IV summarizes the extracted parameters for device B.

Fig. 12(a) shows the measured admittance of device C at room temperature along with the MBVD model fit. The measured A_3 mode shows a resonance at 3.6 GHz and $k_t^2 = 14.6\%$. The measured k_t^2 value is expected to be ~16.5% after deembedding a capacitance of 2.5 fF, which is less than devices A and B as device C has a larger aperture (W_a) resulting in less feedthrough capacitance. Fig. 12(b)

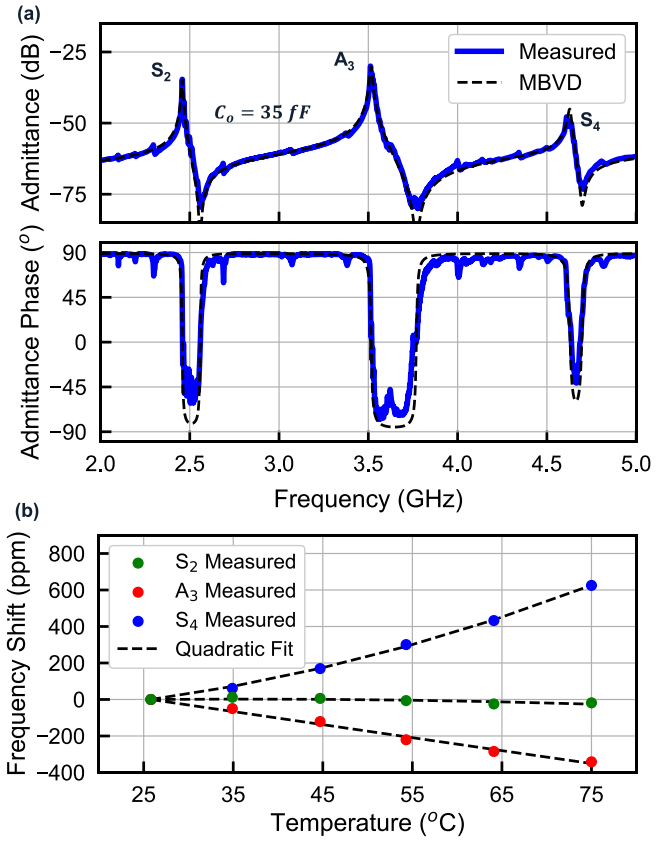

Fig. 11. Measurements of device B. (a) Admittance in magnitude (top) and phase (bottom) along with their MBVD fit. (b) Frequency shift of the acoustic resonator versus temperature for different modes with their quadratic fit used to calculate TCF.

TABLE IV
EXTRACTED PARAMETERS OF DEVICE B

Mode	f_r (GHz)	Q	k_t^2 (%)	TCF (ppm/°C)	TCF_2 (ppm/°C^2)
S_2	2.46	370	13.8	0.41	-0.02
A_3	**3.52**	**400**	**18.1**	**-7.2**	**0.0**
S_4	4.63		2.8	6.72	0.12

TABLE V
EXTRACTED PARAMETERS OF DEVICE C

Mode	f_r (GHz)	Q	k_t^2 (%)	TCF (ppm/°C)	TCF_2 (ppm/°C^2)
S_2	2.51	450	10.7	-13.8	0.09
A_3	**3.63**	**800**	**14.6**	**-17.6**	**-0.03**
S_4	4.72	250	3.5	1.42	0.03

shows the measured resonant frequency deviation for device C in ppm with respect to its value at room temperature. Table V summarizes the extracted parameters for device C.

Measured results, after deembeding the feedthrough effect, are shown in Fig. 6 to verify our FEA simulation model. Small deviations from the simulated values are most likely due to the large range of variation in the bimorph and IDTs thicknesses.

One characteristic of higher order modes is the sensitivity to thickness variation. For the A_3 mode, the simulated

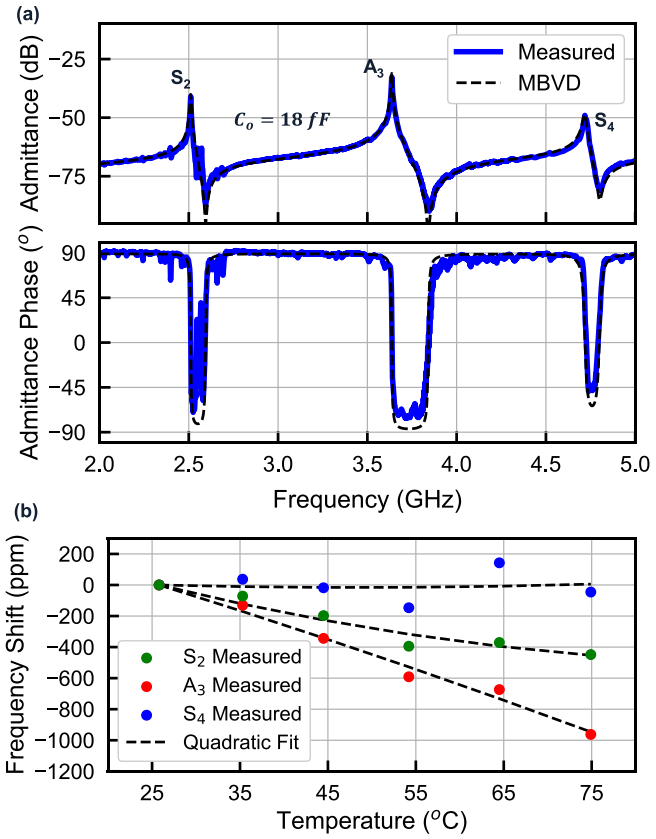

Fig. 12. Measurements of device C. (a) Admittance in magnitude (top) and phase (bottom) along with their MBVD fit. (b) Frequency shift of the acoustic resonator versus temperature for different modes with their quadratic fit used to calculate TCF.

series resonant frequency sensitivity to thickness variations is 4 MHz/nm. This can be seen by comparing Figs. 5(a)–9(a) with 3.6- and 3.5-GHz resonant frequency, respectively, caused by thickness change. Although the value is large, it is still advantageous as it can be used to tune the frequency during fabrication to have multiple resonators with different frequencies on the same substrate. Note that, Lamb waves are highly dispersive when $T/\lambda \ll 1$ and changing λ will not change the frequency. In that case, changing the thickness could be the only way to change the resonant frequency.

IV. Discussion

Targeting a specific k_t^2 or TCF for a specific frequency band can be achieved by selecting the proper resonant mode and controlling the thickness of different materials in the stack. For example, setting $T_{\mathrm{OX}} = 3T_{\mathrm{LN}}$ will maximize the electric field-stress overlap resulting in maximum k_t^2 at S_4 resonant mode and operating at higher frequency ~ 4.7 GHz assuming the same total stack thickness. The same approach can be applied to maximize the coupling at any resonant mode. Moreover, for a specific mode, the thickness of $LiNbO_3$ can be finely controlled by thinning using dry etching applied to the top surface to fine-tune TCF.

In the last fabrication step of releasing the bimorph with XeF_2-based dry etching, considerable residual stress was observed in the $LiNbO_3$ on the SiO_2 stack. Many devices

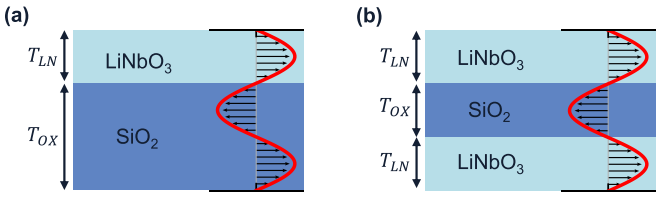

Fig. 13. (a) Bimorph demonstrated in this article resulting in k_t^2 up to 18% for the A_3 mode. (b) Multilayer stack made of two $LiNbO_3$ layers with an intermediate SiO_2 layer expected to produce $k_t^2 > 35\%$ with improved TCF compared to conventional Lamb-wave resonators.

fractured after release, resulting in a meager yield. Considering the mismatch in coefficients of thermal expansion (CTE) of $LiNbO_3$ on SiO_2, the residual stress results from sputtering SiO_2 on Si at 100 °C and bonding $LiNbO_3$ to SiO_2 at room temperature. The few devices that have survived show severe warpage, which most likely results in the spurious response seen in Figs. 9, 11, and 12 (in addition to spurious modes that can be captured by simulations). This spurious response is not acceptable for 5G applications as it appears as intense ripples in the passband. Residual stress and yield improvements are under investigation using other release techniques and better temperature control in fabrication cycles. Further spurious mode mitigation is also under investigation by optimizing lateral dimensions to mitigate lateral spurious modes.

For filter design, use, for example, the ladder topology at the A_3 mode. The series resonant frequency of the series resonator must be aligned to the parallel resonant frequency of the shunt resonator. This alignment is mode-dependent resulting in high insertion loss at S_2 and S_4 modes. Note that those modes are fairly separated from A_3 mode and can be mitigated with lumped elements [51], [52].

A substantial enhancement can be attained using a multilayer stack instead of a bimorph where $LiNbO_3$ can be inserted in different regions with in-phase stress in the thickness direction to maximize the coupling. For example, having two $LiNbO_3$ layers instead of one would approximately double the electromechanical coupling as shown in Fig. 13 for the A_3 mode. FEA simulation of the proposed stack in Fig. 13(b) with similar electrode dimensions to device A resulted in $k_t^2 > 37\%$. Although this approach would result in a more complicated fabrication process, it unlocks opportunities to scale and enhance Lamb-waves acoustic resonators at the same time by customizing materials and their thicknesses in a multilayer stack.

Based on the concepts introduced and verified in this article, Lamb acoustic-wave resonators based on Lamb waves can be designed with frequency scalability, high electromechanical coupling, and improved TCF toward higher performance RF front ends.

V. Conclusion

An acoustic resonator based on Lamb waves was presented in this article. The resonator is based on a bimorph structure made of $LiNbO_3$ and SiO_2, allowing for utilizing higher order Lamb waves with frequency scalability, high electromechanical coupling, and improved TCF simultaneously. Fabricated

devices demonstrated in this article achieved near-zero TCF ~ -1.1 ppm/°C and high electromechanical coupling up to 18% at 3.5 GHz. A significant enhancement to the resonator coupling using a multilayer stack was also introduced. Upon further enhancement, the resonator can be adequate for 5G and IoT applications.

REFERENCES

[1] J. Lee *et al.*, "Spectrum for 5G: Global status, challenges, and enabling technologies," *IEEE Commun. Mag.*, vol. 56, no. 3, pp. 12–18, Mar. 2018.

[2] S. Parkvall, E. Dahlman, A. Furuskar, and M. Frenne, "NR: The new 5G radio access technology," *IEEE Commun. Standards Mag.*, vol. 1, no. 4, pp. 24–30, Dec. 2017.

[3] P. Popovski, K. F. Trillingsgaard, O. Simeone, and G. Durisi, "5G wireless network slicing for eMBB, URLLC, and mMTC: A communication-theoretic view," *IEEE Access*, vol. 6, pp. 55765–55779, 2018.

[4] F. Boccardi, R. W. Heath, Jr., A. Lozano, T. L. Marzetta, and P. Popovski, "Five disruptive technology directions for 5G," *IEEE Commun. Mag.*, vol. 52, no. 2, pp. 74–80, Feb. 2014.

[5] W. Ejaz and M. Ibnkahla, "Multiband spectrum sensing and resource allocation for IoT in cognitive 5G networks," *IEEE Internet Things J.*, vol. 5, no. 1, pp. 150–163, Feb. 2018.

[6] L. Laughlin *et al.*, "Emerging hardware enablers for more efficient use of the spectrum," in *Proc. IEEE Int. Symp. Dyn. Spectr. Access Netw. (DySPAN)*, Newark, NJ, USA, Nov. 2019, pp. 1–9.

[7] T. Kimura, M. Omura, Y. Kishimoto, and K. Hashimoto, "Comparative study of acoustic wave devices using thin piezoelectric plates in the 3–5-GHz range," *IEEE Trans. Microw. Theory Techn.*, vol. 67, no. 3, pp. 915–921, Mar. 2019.

[8] C. Campbell, *Surface Acoustic Wave Devices and Their Signal Processing Applications*. New York, NY, USA: Academic, 1989.

[9] H. Zhang, Q. Yang, W. Pang, J.-G. Ma, and H. Yu, "Temperature stable bulk acoustic wave filters enabling integration of a mobile television function in UMTS system," *IEEE Microw. Wireless Compon. Lett.*, vol. 22, no. 5, pp. 239–241, May 2012.

[10] R. Ruby, "A snapshot in time: The future in filters for cell phones," *IEEE Microw. Mag.*, vol. 16, no. 7, pp. 46–59, Aug. 2015.

[11] O. Kawachi *et al.*, "Optimal cut for leaky SAW on $LiTaO_3$ for high performance resonators and filters," *IEEE Trans. Ultrason., Ferroelectr., Freq. Control*, vol. 48, no. 5, pp. 1442–1448, Sep. 2001.

[12] R. Ruby, "Review and comparison of bulk acoustic wave FBAR, SMR technology," in *Proc. IEEE Int. Ultrason. Symp.*, New York, NY, USA, Oct. 2007, pp. 1029–1040.

[13] T. Takai *et al.*, "I.H.P. SAW technology and its application to microacoustic components (invited)," in *Proc. IEEE Int. Ultrason. Symp. (IUS)*, Washington, DC, USA, Sep. 2017, pp. 1–8.

[14] L. Colombo, A. Kochhar, C. Xu, G. Piazza, S. Mishin, and Y. Oshmyansky, "Investigation of 20% scandium-doped aluminum nitride films for MEMS laterally vibrating resonators," in *Proc. IEEE Int. Ultrason. Symp. (IUS)*, Washington, DC, USA, Sep. 2017, pp. 1–4.

[15] Y. Yang, R. Lu, L. Gao, and S. Gong, "4.5 GHz lithium niobate MEMS filters with 10% fractional bandwidth for 5G front-ends," *J. Microelectromech. Syst.*, vol. 28, no. 4, pp. 575–577, Aug. 2019.

[16] M. Kadota, T. Ogami, K. Yamamoto, Y. Negoro, and H. Tochishita, "High frequency Lamb wave device composed of $LiNbO_3$ thin film," in *Proc. IEEE Ultrason. Symp.*, Beijing, China, Nov. 2008, pp. 1940–1943.

[17] P. J. Turner *et al.*, "5 GHz band n79 wideband microacoustic filter using thin lithium niobate membrane," *Electron. Lett.*, vol. 55, no. 17, pp. 942–944, Aug. 2019.

[18] R. Lu, Y. Yang, M. Breen, M.-H. Li, and S. Gong, "5 GHz acoustic delay lines using antisymmetric mode in lithium niobate thin film," in *Proc. IEEE Int. Ultrason. Symp. (IUS)*, Glasgow, U.K., Oct. 2019, pp. 265–268.

[19] V. Plessky, S. Yandrapalli, P. J. Turner, L. G. Villanueva, J. Koskela, and R. B. Hammond, "5 GHz laterally-excited bulk-wave resonators (XBARs) based on thin platelets of lithium niobate," *Electron. Lett.*, vol. 55, no. 2, pp. 98–100, Jan. 2019.

[20] Y. Yang, A. Gao, R. Lu, and S. Gong, "5 GHz lithium niobate MEMS resonators with high FoM of 153," in *Proc. IEEE 30th Int. Conf. Micro Electro Mech. Syst. (MEMS)*, Las Vegas, NV, USA, Jan. 2017, pp. 942–945.

[21] M. Kadota, T. Ogami, K. Yamamoto, H. Tochishita, and Y. Negoro, "High-frequency Lamb wave device composed of MEMS structure using $LiNbO_3$ thin film and air gap," *IEEE Trans. Ultrason., Ferroelectr., Freq. Control*, vol. 57, no. 11, pp. 2564–2571, Nov. 2010.

[22] S. Gong and G. Piazza, "Design and analysis of lithium–niobate-based high electromechanical coupling RF-MEMS resonators for wideband filtering," *IEEE Trans. Microw. Theory Techn.*, vol. 61, no. 1, pp. 403–414, Jan. 2013.

[23] Y. Yang, R. Lu, and S. Gong, "High Q antisymmetric mode lithium niobate MEMS resonators with spurious mitigation," *J. Microelectromech. Syst.*, vol. 29, no. 2, pp. 135–143, Apr. 2020.

[24] R. Lu, Y. Yang, S. Link, and S. Gong, "A1 resonators in 128° Y-cut lithium niobate with electromechanical coupling of 46.4%," *J. Microelectromech. Syst.*, vol. 29, no. 3, pp. 313–319, Jun. 2020.

[25] Q. Zou *et al.*, "High coupling coefficient temperature compensated FBAR resonator for oscillator application with wide pulling range," in *Proc. IEEE Int. Freq. Control Symp.*, Newport Beach, CA, USA, Jun. 2010, pp. 646–651.

[26] H. Nakanishi, H. Nakamura, T. Tsurunari, J. Fujiwara, Y. Hamaoka, and K. Hashimoto, "Good temperature coefficient of frequency SAW resonator on a SiO_2/Al/$LiNbO_3$ structure," in *Proc. IEEE Int. Ultrason. Symp.*, San Diego, CA, USA, Oct. 2010, pp. 1298–1301.

[27] Y. Wang *et al.*, "A zero TCF band 13 SAW duplexer," in *Proc. IEEE Int. Ultrason. Symp. (IUS)*, Taipei, Taiwan, Oct. 2015, pp. 1–4.

[28] T. Nishihara, S. Taniguchi, and M. Ueda, "Increased piezoelectric coupling factor in temperature-compensated film bulk acoustic resonators," in *Proc. IEEE Int. Ultrason. Symp. (IUS)*, Taipei, Taiwan, Oct. 2015, pp. 1–4.

[29] H. Kando *et al.*, "Plate wave resonator using rotated Y-cut single crystal $LiTaO_3$ thin film made by ion implant technology," in *Proc. Asia–Pacific Microw. Conf.*, Yokohama, Japan, 2010, pp. 920–923.

[30] T. Kimura, K. Daimon, T. Ogami, and M. Kadota, "S0 mode Lamb wave resonators using $LiNbO_3$ thin plate on acoustic multilayer reflector," *Jpn. J. Appl. Phys.*, vol. 52, no. 7S, Jul. 2013, Art. no. 07HD03.

[31] C.-M. Lin *et al.*, "Temperature-compensated aluminum nitride Lamb wave resonators," *IEEE Trans. Ultrason., Ferroelectr., Freq. Control*, vol. 57, no. 3, pp. 524–532, Mar. 2010.

[32] L. Shi and G. Piazza, "Lithium niobate on silicon dioxide suspended membranes: A technology platform for engineering the temperature coefficient of frequency of high electromechanical coupling resonators," *J. Microelectromech. Syst.*, vol. 23, no. 6, pp. 1318–1329, Dec. 2014.

[33] A. Boes, B. Corcoran, L. Chang, J. Bowers, and A. Mitchell, "Status and potential of lithium niobate on insulator (LNOI) for photonic integrated circuits," *Laser Photon. Rev.*, vol. 12, no. 4, Apr. 2018, Art. no. 1700256.

[34] M.-H. Li, C.-Y. Chen, R. Lu, Y. Yang, T. Wu, and S. Gong, "Temperature stability analysis of thin-film lithium niobate SH0 plate wave resonators," *J. Microelectromech. Syst.*, vol. 28, no. 5, pp. 799–809, Oct. 2019.

[35] A. E. Hassanien, R. Lu, and S. Gong, "Near zero TCF acoustic resonator with high electromechanical coupling of 13.5% at 3.5 GHz," in *Proc. IEEE Int. Microw. Symp. (IMS)*, Atlanta, GA, USA, 2021.

[36] B. A. Auld, *Acoustic Fields and Waves in Solids*, vol. 2. Hoboken, NJ, USA: Wiley, 1973.

[37] D. Royer and E. Dieulesaint, *Elastic Waves in Solids: Free and Guided Propagation*. Berlin, Germany: Springer, 1996.

[38] R. S. Weis and T. K. Gaylord, "Lithium niobate: Summary of physical properties and crystal structure," *Appl. Phys. A Solids Surf.*, vol. 37, no. 4, pp. 191–203, Aug. 1985.

[39] S. Gong, "Lithium niobate for M/NEMS resonators," in *Piezoelectric MEMS Resonators*, H. Bhugra and G. Piazza, Eds. Cham, Switzerland: Springer, 2017, pp. 99–129.

[40] K. Hashimoto, *RF Bulk Acoustic Wave Filters for Communications*. Norwood, MA, USA: Artech House, 2009.

[41] S. H. Chang, N. N. Rogacheva, and C. C. Chou, "Analysis of methods for determining electromechanical coupling coefficients of piezoelectric elements," *IEEE Trans. Ultrason., Ferroelectr., Freq. Control*, vol. 42, no. 4, pp. 630–640, Jul. 1995.

[42] K. Shibayama, K. Yamanouchi, H. Sato, and T. Meguro, "Optimum cut for rotated Y-cut $LiNbO_3$ crystal used as the substrate of acoustic-surface-wave filters," *Proc. IEEE*, vol. 64, no. 5, pp. 595–597, May 1976.

[43] H. Goldstein, C. Poole, J. Safko, and S. R. Addison, *Classical Mechanics*, 3rd ed. London, U.K.: Pearson, 2014.

[44] D. Morgan, *Surface Acoustic Wave Filters*. Amsterdam, The Netherlands: Elsevier, 2007.

[45] R. Lu, T. Manzaneque, Y. Yang, M.-H. Li, and S. Gong, "Gigahertz low-loss and wideband S0 mode lithium niobate acoustic delay lines," *IEEE Trans. Ultrason., Ferroelectr., Freq. Control*, vol. 66, no. 8, pp. 1373–1386, Aug. 2019.
[46] *IEEE Standard on Piezoelectricity*, Amer. Nat. Standard Inst., New York, NY, USA, 1978.
[47] R. Lu, M.-H. Li, Y. Yang, T. Manzaneque, and S. Gong, "Accurate extraction of large electromechanical coupling in piezoelectric MEMS resonators," *J. Microelectromech. Syst.*, vol. 28, no. 2, pp. 209–218, Apr. 2019.
[48] N. F. Naumenko, "Optimal orientations of $LiTaO_3$ for application in plate mode resonators," *J. Appl. Phys.*, vol. 118, no. 3, Jul. 2015, Art. no. 034505.
[49] J. D. Larson, P. D. Bradley, S. Wartenberg, and R. C. Ruby, "Modified Butterworth-Van Dyke circuit for FBAR resonators and automated measurement system," in *Proc. IEEE Int. Ultrason. Symp.*, San Juan, PR, USA, vol. 1, Oct. 2000, pp. 863–868.
[50] M. Levy *et al.*, "Fabrication of single-crystal lithium niobate films by crystal ion slicing," *Appl. Phys. Lett.*, vol. 73, no. 16, pp. 2293–2295, Oct. 1998.
[51] Y. Yang, L. Gao, and S. Gong, "X-band miniature filters using lithium niobate acoustic resonators and bandwidth widening technique," *IEEE Trans. Microw. Theory Techn.*, vol. 69, no. 3, pp. 1602–1610, Mar. 2021.
[52] L. Gao, Y. Yang, and S. Gong, "Wideband hybrid monolithic lithium niobate acoustic filter in the K-band," *IEEE Trans. Ultrason., Ferroelectr., Freq. Control*, vol. 68, no. 4, pp. 1408–1417, Apr. 2021.

Ahmed E. Hassanien (Student Member, IEEE) received the B.Sc. degree (Hons.) and the M.Sc. degree in electronics and communications engineering from Ain Shams University, Cairo, Egypt, in 2011 and 2016, respectively. He is currently pursuing the Ph.D. degree at the University of Illinois at Urbana–Champaign (UIUC), Urbana, IL, USA. During his M.Sc. degree, he worked on energy harvesting from mechanical vibration using piezoelectric MEMS devices. Since 2017, he has been working on various topics toward his Ph.D., including mechanical antennas, microwave filters, acoustic resonators, scanning mirrors, and integrated photonics.

From 2011 to 2015, he worked as a full-time Product Engineer at Si-Ware Systems (SWS), Cairo, while working on his M.Sc. From 2015 to 2017, he worked for Mentor Graphics (now Siemens EDA) as an IC Design Consultant.

Mr. Ahmed was a recipient of the 2018 Dr. Ok Kyun Kim Fellowship from the Department of Electrical and Computer Engineering, UIUC, and the 2020 Mavis Future Faculty Fellowship from the College of Engineering, UIUC.

Ruochen Lu (Member, IEEE) received the B.E. degree (Hons.) in microelectronics from Tsinghua University, Beijing, China, in 2014, and the M.S. and Ph.D. degrees in electrical engineering from the University of Illinois at Urbana–Champaign, Urbana, IL, USA, in 2017 and 2019, respectively.

He is an Assistant Professor with the Department of Electrical and Computer Engineering, The University of Texas at Austin, Austin, TX, USA. His research primarily focuses on developing chip-scale acoustic and electromagnetic components and microsystems for RF applications. His work aims to demonstrate reconfigurable and tunable RF functions using novel MEMS platforms, toward higher operating frequencies and more efficient transduction between the EM and acoustic domains. In addition, he works on ultrasonic transducers and multiphysics hybrid microsystems for signal processing, sensing, and computing applications.

Songbin Gong (Senior Member, IEEE) received the Ph.D. degree in electrical engineering from the University of Virginia, Charlottesville, VA, USA, in 2010.

He is currently an Associate Professor and the Intel Alumni Fellow with the Department of Electrical and Computer Engineering and the Micro and Nanotechnology Laboratory, University of Illinois at Urbana–Champaign, Urbana, IL, USA. His current research interests include the design and implementation of radio frequency microsystems, components, and subsystems for reconfigurable RF front ends. In addition, his research explores hybrid microsystems based on the integration of MEMS devices with photonics or circuits for signal processing and sensing.

Dr. Gong was a recipient of the 2014 Defense Advanced Research Projects Agency Young Faculty Award, the 2017 NASA Early Career Faculty Award, the 2019 UIUC College of Engineer Dean's Award for Excellence in Research, and the 2019 Ultrasonics Early Career Investigator Award. Along with his students and postdoctorals, he received the Best Paper Awards from the 2017 and 2019 IEEE International Frequency Control Symposium, the 2018 and 2019 International Ultrasonics Symposium, and the Second Place in the Best Paper Competition at the 2018 IEEE International Microwave Symposium. He is a Technical Committee Member of MTT-21 RF-MEMS of the IEEE Microwave Theory and Techniques Society, the International Frequency Control Symposium, and the International Electron Devices Meeting. He serves as the Chair for MTT TC2 and TC 21 and an Associate Editor for the IEEE TRANSACTIONS ON ULTRASONICS, FERROELECTRICS, AND FREQUENCY CONTROL.